

# Interfacial Model Deciphering High-Voltage Electrolytes for High Energy Density, High Safety, and Fast-Charging Lithium-Ion Batteries

Yeguo Zou, Zhen Cao, Junli Zhang,\* Wandi Wahyudi, Yingqiang Wu, Gang Liu, Qian Li, Haoran Cheng, Dongyu Zhang, Geon-Tae Park, Luigi Cavallo, Thomas D. Anthopoulos, Limin Wang, Yang-Kook Sun,\* and Jun Ming\*

High-voltage lithium-ion batteries (LIBs) enabled by high-voltage electrolytes can effectively boost energy density and power density, which are critical requirements to achieve long travel distances, fast-charging, and reliable safety performance for electric vehicles. However, operating these batteries beyond the typical conditions of LIBs (4.3 V vs Li/Li<sup>+</sup>) leads to severe electrolyte decomposition, while interfacial side reactions remain elusive. These critical issues have become a bottleneck for developing electrolytes for applications in extreme conditions. Herein, an additive-free electrolyte is presented that affords high stability at high voltage (4.5 V vs Li/Li<sup>+</sup>), lithium-dendrite-free features upon fast-charging operations (e.g., 162 mAh g<sup>-1</sup> at 3 C), and superior long-term battery performance at low temperature. More importantly, a new solvation structure-related interfacial model is presented, incorporating molecular-scale interactions between the lithium-ion, anion, and solvents at the electrolyte–electrode interfaces to help interpret battery performance. This report is a pioneering study that explores the dynamic mutual-interaction interfacial behaviors on the lithium layered oxide cathode and graphite anode simultaneously in the battery. This interfacial model enables new insights into electrode performances that differ from the known solid electrolyte interphase approach to be revealed, and sets new guidelines for the design of versatile electrolytes for metal-ion batteries.

handheld electronics and electric vehicles.<sup>[1]</sup> However, the current LIBs cannot satisfy growing demands for higher energy density, greater power capability, and the better safety performances required for large-scale applications.<sup>[2]</sup> Although high-capacity and/or high-voltage cathodes (e.g., Ni-rich, Li-rich layered oxides,<sup>[3]</sup> and spinel LiNi<sub>0.5</sub>Mn<sub>1.5</sub>O<sub>4</sub> cathodes<sup>[4]</sup>), as well as high-capacity anodes (e.g., Li-,<sup>[5]</sup> Si-,<sup>[6]</sup> and Sn<sup>[7]</sup>-based materials), are being widely explored, the issue of developing a compatible electrolyte for these electrodes has become ever more important.<sup>[8]</sup> Particularly in extreme conditions (e.g., high-voltage, low/high temperature, and super-fast charging/discharging), detrimental electrolyte–electrode side reactions are inevitable because electrolyte-determined interfacial stability as a precondition for battery operations is still not yet fully understood.<sup>[9]</sup> For example, a severe electrolyte decomposition occurs on the surface of electrodes upon charging LIBs at a high voltage (≥4.5 V vs Li/Li<sup>+</sup>).<sup>[10]</sup> To this end, designing electrolytes by stabilizing the electrolyte–electrode interfaces

has attracted great attention to enable boosting of high energy density, fast-charging time, and high-power density batteries.

Unfortunately, conventional ethylene carbonate (EC)-based electrolytes are oxidized on the highly active surface of


## 1. Introduction

Lithium-ion batteries (LIBs) have become an indispensable energy storage technology and play an important role in

Y. Zou, Y. Wu, G. Liu, Q. Li, H. Cheng, D. Zhang, L. Wang, J. Ming  
State Key Laboratory of Rare Earth Resource Utilization  
Changchun Institute of Applied Chemistry  
CAS  
Changchun 130022, China  
E-mail: jun.ming@ciac.ac.cn

Y. Zou, G. Liu, H. Cheng, D. Zhang, L. Wang, J. Ming  
University of Science and Technology of China  
Hefei 230026, China

Z. Cao, W. Wahyudi, L. Cavallo, T. D. Anthopoulos  
Physical Science and Engineering Division (PSE)  
King Abdullah University of Science and Technology (KAUST)  
Thuwal 23955-6900, Saudi Arabia

 The ORCID identification number(s) for the author(s) of this article can be found under <https://doi.org/10.1002/adma.202102964>.

DOI: 10.1002/adma.202102964

J. Zhang  
Key Laboratory of Magnetism and Magnetic Materials of the  
Ministry of Education  
School of Physical Science and Technology  
Lanzhou University  
Lanzhou 730000, China  
E-mail: zhangjl@lzu.edu.cn

G.-T. Park, Y.-K. Sun  
Department of Energy Engineering  
Hanyang University  
Seoul 133-791, Republic of Korea  
E-mail: yksun@hanyang.ac.kr

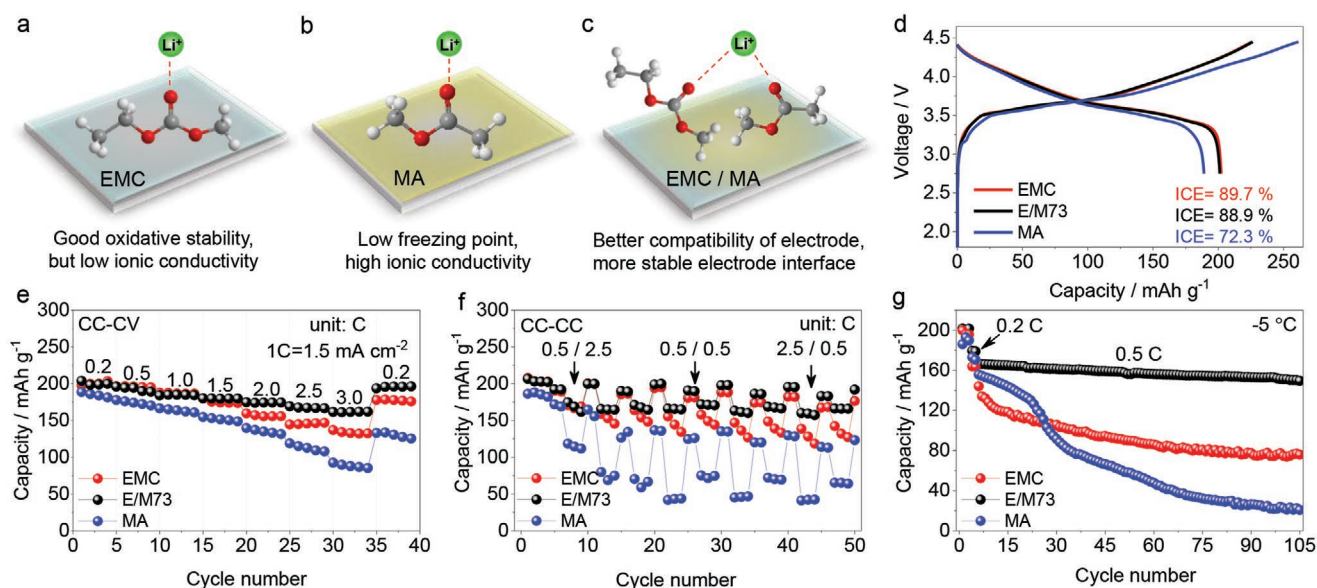


**Figure 1.** Characteristics of solvents and battery performance in different electrolytes. a) Linear carbonate (EMC), b) linear carboxylate (MA), and c) binary solvent-based (EMC/MA) electrolytes. Comparative electrochemical performance of different electrolytes in the graphite || NCM622 cell at the high voltage of 4.45 V. d) Voltage versus capacity profile and initial Coulombic efficiency (ICE) in the first cycle, e) rate performance, f) special fast charging/discharging feature, and g) long-term cycling at  $-5\text{ }^{\circ}\text{C}$  under 0.5 C ( $C = 1.5\text{ mA cm}^{-2}$ ).

cathodes upon battery operation at high potential ( $\geq 4.3\text{ V vs Li/Li}^+$ ).<sup>[11]</sup> EC was found to react with the singlet oxygen that was released from the  $\text{LiNi}_x\text{Co}_y\text{Mn}_z$  ( $x + y + z = 1$ , i.e., NCM cathode),<sup>[12]</sup> and/or bring a transfer of atomic hydrogen from EC.<sup>[13]</sup> Thus, numerous efforts have been devoted to the development of electrolytes without using EC solvent, such as super-concentrated electrolytes,<sup>[14]</sup> localized high-concentration electrolytes,<sup>[15]</sup> and all-fluorinated electrolytes.<sup>[16]</sup> Improved battery performances upon the use of these new electrolyte systems are mainly ascribed to the formation of a robust cathode-electrolyte interface (CEI) film that helps to suppress electrolyte decomposition. This viewpoint is similar to adding film-forming additives (e.g., vinylene carbonate, prop-1-ene-1,3-sultone, and triallyl phosphate) in EC-free electrolytes.<sup>[17]</sup> However, the molecular-scale interactions of the lithium-ion ( $\text{Li}^+$ ), anion, and solvent on the electrolyte-electrode interfaces are not fully understood, while their effects on  $\text{Li}^+$  transport, electrochemical stability of the electrolyte, and electrode performance also remain elusive. Therefore, to the best of our knowledge, there are no clear interfacial chemistry guidelines for designing electrolytes to improve battery performance, besides the well-known consensus of CEI formation.

The lack of clear guidelines (i.e., a focus on addressing the challenges on the cathode only) has resulted in new problems at the anode. Many overlooked problems on the anode have been reported when an EC solvent-free strategy is employed to avoid electrolyte oxidation on the cathode. For example, serious side-effects from severe decay of cycle performance and safety issues with LIBs have been reported when using EC-free electrolyte<sup>[18]</sup> because the lithium metal is plated on the graphite anode readily during the fast charging or high-rate cycling due to the absence of EC solvent. Thus, an in-depth understanding of molecular-scale interfacial behaviors and reaction mechanisms on the surface of electrodes, particularly the cathode and anode simultaneously, is crucial for developing electrolytes.

Herein, a new carbonate-based high-voltage electrolyte employing a mixture of ethyl methyl carbonate (EMC) and methyl acetate (MA) solvents without adding any additive is reported. The electrolyte successfully achieves excellent stability, fast-charging capability, and superior low-temperature performances of LIBs at a normal concentration of 1.2 M  $\text{LiPF}_6$ . It is confirmed that the interactions between the lithium-ion, anion, and solvent play a critical role to determine the interfacial behaviors between the electrolyte and electrodes. Based on these findings, a new interfacial model is presented to explain the stability of the electrolyte on the surface of the NCM cathode and graphite anode. This work significantly complements our understanding of solid electrolyte interphase (i.e., SEI or CEI) effects on battery performance. More importantly, the interfacial model presented provides an efficient strategy for engineering the solid-liquid interfacial chemistry by regulating the solvation structure, which is crucial for a wide range of metal-ion battery systems.

## 2. Result and Discussion

### 2.1. Features of High-Voltage Electrolyte

The newly designed high-voltage electrolyte is composed of EMC and MA solvents, in which EMC has a good oxidative stability (Figure 1a)<sup>[19]</sup> and MA has a low freezing point and a high ionic conductivity (Figure 1b).<sup>[20]</sup> While EMC can guarantee high electrolyte stability at high voltage, MA can overcome the disadvantages of EMC (i.e., low ionic conductivity and dielectric constant)<sup>[21]</sup> to enhance the ionic conductivity for greater rate capabilities, especially in low-temperature conditions (Figure 1c). As a paradigm, the graphite || NCM622 battery employing this high voltage electrolyte (i.e., EMC/MA = 7/3 v/v, E/M73) demonstrates a high initial Coulombic efficiency (ICE)

of 88.9% and a capacity of 201.2 mAh g<sup>-1</sup>, which is close to that when employing EMC electrolyte (89.7%, 202.3 mAh g<sup>-1</sup>) but much higher than that when employing MA electrolyte (72.3%, 189 mAh g<sup>-1</sup>) at a high voltage of 4.45 V (Figure 1d, see battery configuration in Figure S1, Supporting Information). This result is consistent with the higher stability of the E/M73 electrolyte, as confirmed by linear sweep voltammograms and step-wise potential sweep measurements<sup>[22]</sup> in Figure S2, Supporting Information. Moreover, the comparative cycle performance of the cell employing different electrolytes also corroborates this observation (Figure S3a–c, Supporting Information).

A high wettability of electrolytes also contributes to the power capacity of the cell. It was found that the contact angles of E/M73 electrolyte on the NCM622 cathode, PP separator, and graphite anode were 9.1°, 30.6°, and 8.2°, respectively, which is lower than that of EMC (9.7°, 33.3°, and 9.4°) and E/E73 (i.e., the commercial electrolyte of 1.2 M LiPF<sub>6</sub> in EMC:EC = 7:3 (v:v); 13.9°, 41.7°, and 12.8°) (Figure S4, Supporting Information). This result should benefit from the low viscosity of MA solvent (i.e., 0.364 mPa s<sup>-1</sup>). Then, a much higher power density can be obtained by employing the E/M73 electrolyte (Figure 1e). For example, the battery achieves capacities of 175, 170, and 162 mAh g<sup>-1</sup> at a rate of 2.0, 2.5, and 3.0 C, which is much higher than those employing EMC (i.e., 160, 145, and 137 mAh g<sup>-1</sup>) and MA (i.e., 140, 119, and 93 mAh g<sup>-1</sup>) electrolytes. The initial discharge and power capacities obtained are greatly improved compared to high-voltage LIBs using different previously reported electrolytes (Table S1, Supporting Information). Furthermore, the capacity is successfully retained at 197 mAh g<sup>-1</sup> at 0.2 C after the high C-rate test, which is more improved than that of 176 and 125 mAh g<sup>-1</sup> by employing EMC and MA electrolytes, respectively. Moreover, it was also confirmed that the cycle performance (i.e., a capacity retention of 89.0% after 100 cycles at 1.9 mA cm<sup>-2</sup>) and power capacity (i.e., 150.4 mAh g<sup>-1</sup> at 3 C) were well-maintained even at a high mass loading of active materials (Figure S3d,e, Supporting Information), demonstrating the practical capabilities of the electrolyte.

The fast-charging features of our electrolyte were further demonstrated by a fast Constant Current–Constant Current protocol (Figure 1f). It was found that 81.2% of the initial capacity was achieved under 2.5 C (i.e., 24 min) using E/M73 electrolyte, the value of which is higher than the 71.7% and 41.1% of the cells employing EMC and MA electrolytes. These criteria meet the fast-charging application standards stations well (e.g., 120 kW-Tesla Supercharger recharges 80% SOC in 40 min).<sup>[23]</sup> Moreover, our electrolyte retains 89.8% of the initial capacity at 0.5 C after 100 cycles under a low-temperature measurement of –5 °C, which is also much higher than the values of 56.2% and 13.4% obtained with EMC and MA electrolytes (Figure 1g). These results confirm the specialness of E/M73 high-voltage electrolyte, which enables a superior power capability and low-temperature performance at a high-voltage operation.

Note that high-temperature performance deteriorated by the MA solvent is maximally suppressed by the EMC solvent in E/M73 electrolyte, where EMC has a positive effect likely additive.<sup>[24]</sup> The capacity retention of the cell is 85.4% after 50 cycles at 1 C when the cell was cycled at 50 °C (Figure S3c, Supporting Information). The performance of the cell at high temperature is even better than that employing the EMC electrolyte, while it is slightly

reduced compared to that at room temperature (Figure S3b, Supporting Information). This result should be mainly attributed to the change in the interaction between PF<sub>6</sub><sup>-</sup> and Li<sup>+</sup> at high temperatures, where it is easier for PF<sub>6</sub><sup>-</sup> to reach the surface of the cathode and induce the solvent dehydrogenation. A detailed interpretation of this viewpoint is discussed in the interfacial model in Section 2.7. Moreover, the thermal stability of the mixture of de-lithiated NCM622 cathode and electrolyte was studied by differential scanning calorimetry.<sup>[25]</sup> It was found that the onset/peak temperature of the main peaks in the E/M73 electrolyte could be maintained at 219.9 °C/238.1 °C, which is much higher than 203.8 °C/214.5 °C for the MA electrolyte and 217.7 °C/222.5 °C for the commercial E/E73 electrolyte. This finding suggests that the thermal runaway reactions of the E/M73 electrolyte can be also suppressed at high potential, likely in the EMC electrolyte (i.e., 253.3 °C/255.7 °C). The results demonstrate that the disadvantages of the MA solvent could be overcome maximally by the EMC solvent from the aspects of bulk electrolyte and interfacial chemistry, as discussed later.

## 2.2. Electrode Impedance Analysis

The foundation of the high performance of the electrolyte was investigated by hybrid pulse power characterization (HPPC) and electrochemical impedance spectroscopy (EIS) measurements. The area-specific impedance (ASI) change of HPPC was the most direct technique to compare battery power characteristics (Figure S5, Supporting Information).<sup>[26]</sup> The ASI values, calculated using Equation (1)

$$R_{disc} = (V_0 - V_1) / I_{disc} \quad (1)$$

and the corresponding depth of discharge (OCV) in different electrolytes are shown in Figure 2a–c. The average impedance of the full cell employing E/M73 electrolyte increased slightly from 59.9 to 64.4 Ω cm<sup>2</sup> after five HPPC cycles, while the corresponding values in the EMC and MA electrolytes increased from 75.4 to 82.2 Ω cm<sup>2</sup> and from 96.1 to 106.4 Ω cm<sup>2</sup>, respectively. This finding demonstrates that the ohmic and concentration polarization are very low in the E/M73 electrolyte. In addition, the corresponding OCVs of the E/M73 electrolytes under various DODs were also the most stable compared to those of EMC and MA electrolytes (Figure 2a–c).

The EIS test was further employed to explore the interfacial impedance evolution of the full battery upon cycling (Figure 2d–f and Table S2, Supporting Information). The *R*(*Z*) impedance of the full cell employing the EMC (94.7 Ω cm<sup>2</sup>) and E/M73 (92.2 Ω cm<sup>2</sup>) electrolytes was similar after 200 cycles. In contrast, the value was higher in the full cell employing MA electrolytes (128.6 Ω cm<sup>2</sup>) (Figure 2d), showing the same trend as their cycling performance (Figure S3b, Supporting Information). The origins of the impedance were analyzed from the *R*(*Z*) impedance of the symmetric NCM622 || NCM622 and graphite || graphite cells. It was found that the impedance of the symmetric NCM622 || NCM622 cell using E/M73 electrolyte (176.8 Ω cm<sup>2</sup>) was slightly higher than that using EMC electrolyte (166.6 Ω cm<sup>2</sup>), which was much lower than that using MA electrolyte (267.3 Ω cm<sup>2</sup>) (Figure 2e). This result



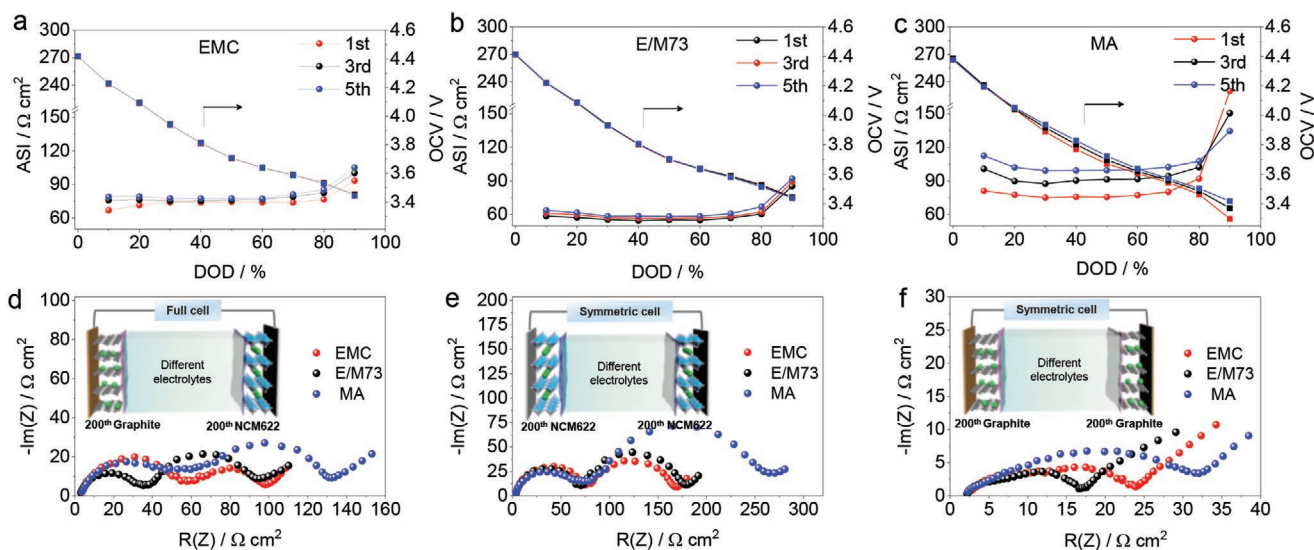


**Figure 2.** Comparison of power feature and interfacial impedance. Comparative ASI impedance and OCVs of the graphite || NCM622 cell by the HPPC used a) EMC, b) E/M73, and c) MA electrolytes. EIS impedance of d) graphite || NCM622 full cell and the symmetrical cell of e) NCM622 || NCM622 and f) graphite || graphite in different electrolytes after 200 cycles at 1 C.

demonstrates that EMC is more compatible with the cathode at high voltage, while the amount of MA needs to be controlled prudently due to its low stability. More significant differences were observed on the cycled graphite anode. The  $R(Z)$  impedance of symmetric graphite || graphite cells employing E/M73 electrolyte was about  $14.4 \Omega \text{ cm}^2$  after 200 cycles, which is much lower than the  $21.1$  and  $29.8 \Omega \text{ cm}^2$  of that using EMC and MA electrolytes (Figure 2f), respectively. This result shows that the electrolyte decomposition on the graphite anode could be mitigated by E/M73 electrolyte. The impedance analysis shows that different electrolyte decomposition occurs on the surface of electrodes, giving rise to different SEI formations. However, the role of electrolyte composition in the electrolyte decomposition that occurs on the surface of electrodes needs to be further studied at the molecular scale.

### 2.3. Electrolyte/Cathode Interface

The morphology and crystalline structure of the cycled NCM622 cathodes were investigated to understand the origin of the different performances of the electrolytes (Figure 3). It was found that the secondary particles were intact and distributed evenly on the cycled NCM622 electrodes when the EMC and E/M73 electrolytes were used (Figure 3a–a<sub>2</sub>). The only difference was a little deposition observed on the smooth surface of NCM622 particles cycled with the E/M73 electrolyte (Figure 3b–b<sub>2</sub> and Figure S6a, Supporting Information). In contrast, microcracking in the secondary particles and more decomposition products were observed on the surface of the primary particles upon the use of MA electrolyte (Figure 3c–c<sub>2</sub>). This observation is consistent with the impedance analysis (Figure 2e), demonstrating the durability of the EMC solvent for the cathodes.

X-ray photoelectron spectroscopy (XPS) analysis further confirmed the different components of decomposed electrolytes on the surface of NCM622 cathodes. There is a similar

component of O-lattice ( $529.3 \text{ eV}$ ),<sup>[27]</sup> C=O ( $532 \text{ eV}$ ), and C–O groups ( $533.7 \text{ eV}$ )<sup>[28]</sup> on the cathodes cycled with EMC and E/M73 electrolytes (Figure 3d). In contrast, the amount of C=O was dominant while the O-lattice was absent on the surface of the cathode cycled with MA electrolyte (Figure S7a, Supporting Information), which is because the MA solvent is decomposed to form lithium alkyl carbonates and carbonate salt readily and then covers the surface of the NCM622 cathode. Then, the signal of O-lattice on the NCM622 may be covered so that the spectra are difficult to detect. More information could be summarized from the F 1s spectra, in which the peaks at  $687.8$ ,  $686.6$ , and  $685.1 \text{ eV}$  correspond to the PVDF binder,<sup>[10]</sup>  $\text{Li}_x\text{PO}_y\text{F}_z$  (i.e., the decomposition products of  $\text{LiPF}_6$ ),<sup>[27]</sup> and  $\text{LiM}_x\text{F}_y\text{O}_z$  ( $M = \text{Ni, Co, or Mn}$ ) (i.e., formed by reacting with HF),<sup>[29]</sup> respectively (Figure 3e). It was found that the relative content of  $\text{LiM}_x\text{F}_y\text{O}_z$  increased (Figure S7b, Supporting Information) with increasing the volume of MA, which is due to the content of the HF (i.e., it is generated by reacting protic species from the dehydrogenation of solvents with  $\text{LiPF}_6$ ) being increased in the MA electrolyte. In other words, the dehydrogenation of solvents and the oxidative decomposition of  $\text{LiPF}_6$  were suppressed in EMC and E/M73 electrolytes; thus the amount of  $\text{Li}_x\text{PO}_y\text{F}_z$  in CEI becomes dominant compared to the  $\text{LiM}_x\text{F}_y\text{O}_z$ .

The crystallographic variation of the NCM622 cathodes was further analyzed by the peak shifts of (003) scattering angles in XRD patterns (Figure 3f). The peak of (003) was shifted to a lower angle in the cathode cycled with the MA electrolyte, demonstrating increased crystal plane cracks caused by local structural collapse. This could be ascribed to serious MA electrolyte decomposition, in which side reactions can corrode the electrode and cause structural degradation. The local structural change of the NCM622 cathode under the high-resolution transmission electron microscope provides more evidence (Figure 3g–j), in which the layered (i.e.,  $R\text{-}3m$  space group<sup>[30]</sup>) and partial spinel phases coexist in the inner and outer surface area on the NCM622 electrode cycled with the EMC electrolyte

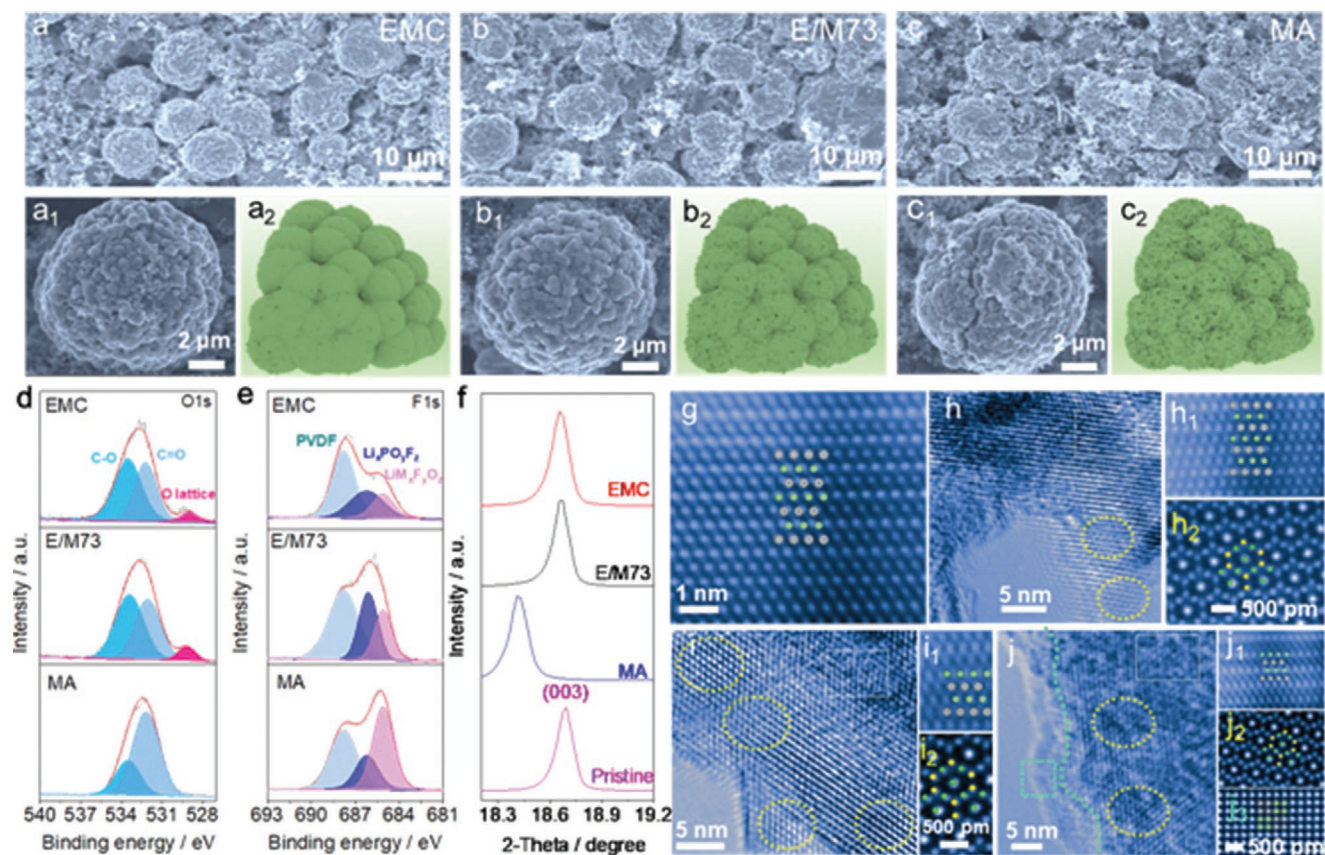


**Figure 3.** Characterizations of NCM622 cathode in the graphite || NCM622 cell employing different electrolytes after 200 cycles. SEM images and illustration of the cycled NCM622 particles from a–a<sub>2</sub>) EMC, b–b<sub>2</sub>) E/M73, and c–c<sub>2</sub>) MA electrolytes. XPS spectra of d) O 1s and e) F 1s of the cycled NCM622 electrode. XRD patterns of f) (003) peak and HRTEM images of NCM622 surface layer from g) pristine, h–h<sub>2</sub>) EMC, i–i<sub>2</sub>) E/M73, and j–j<sub>2</sub>) MA electrolytes.

(Figure 3h<sub>1</sub>,h<sub>2</sub>). In contrast, the spinel phases increased slightly with the E/M73 electrolyte (Figure 3i<sub>2</sub>), while rock-salt phases (Ni–O)<sup>[31]</sup> could be also detected in the MA electrolyte (Figure 3j<sub>3</sub>). This result demonstrates the necessity of adding EMC into MA to protect the NCM cathode, otherwise, the high-valence Ni<sup>4+</sup> and Ni<sup>3+</sup> ions formed in a fully charged state could be easily reduced to Ni<sup>2+</sup> ions by MA. The highly active oxidative Ni<sup>4+</sup> and electrolytes decomposition products, such as HF, could form an exceptionally unstable environment under the high-voltage charge.<sup>[32]</sup> This process could trigger a severe oxygen evolution from the electrode, induce phase transformation, and further exacerbate the electrolyte decomposition.

#### 2.4. Electrolyte/Anode Interface Analysis

The interaction between the electrolyte and graphite anode is also important in full batteries, especially during cycling at fast charging and high voltage. The variation in the cycled graphite anodes with different electrolytes is investigated in Figure 4. Lithium deposition and electrolyte decomposition were observed on the surface of cycled graphite using the EMC electrolyte (Figure 4a,d vs Figure S6b, Supporting Information). The findings are due to the high concentration polarization

of EMC electrolytes and the reactivity between lithium metal and EMC solvent. In contrast, the lithium deposition and electrolyte decomposition on the surface of the graphite anode were significantly mitigated by using the E/M73 electrolyte (Figure 4b,e). These results are consistent with the impedance analysis (Figure 2f). The observations of graphite cycled with the MA electrolyte lay in an intermediate position between the EMC and E/M73 electrolytes (Figure 4c,f). The compatibility of electrolytes judged from the cycled graphite anodes is in the sequence E/M73 > MA > EMC, which was further proven by the stability of the symmetric Li || Li cells (Figure S8, Supporting Information). These results demonstrate the necessity of MA addition into the EMC electrolyte to ensure good compatibility with the graphite anode, which significantly suppresses lithium deposition and electrolyte decomposition. Although EMC demonstrates good compatibility with the NCM622 cathode at high voltage, EMC could react with fresh lithium readily on the graphite anode surface and cause severe capacity decay (Figure S3b, Supporting Information).

These observations were further confirmed by XPS analysis of the electrolyte decomposition products on the graphite anodes. The LiCO<sub>3</sub> peaks in C 1s spectra (i.e., 289.9 eV)<sup>[33]</sup> and Li 1s spectra (i.e., 55.3 eV vs LiF at 56.0 eV)<sup>[34]</sup> significantly increase on the graphite cycled with the EMC electrolyte



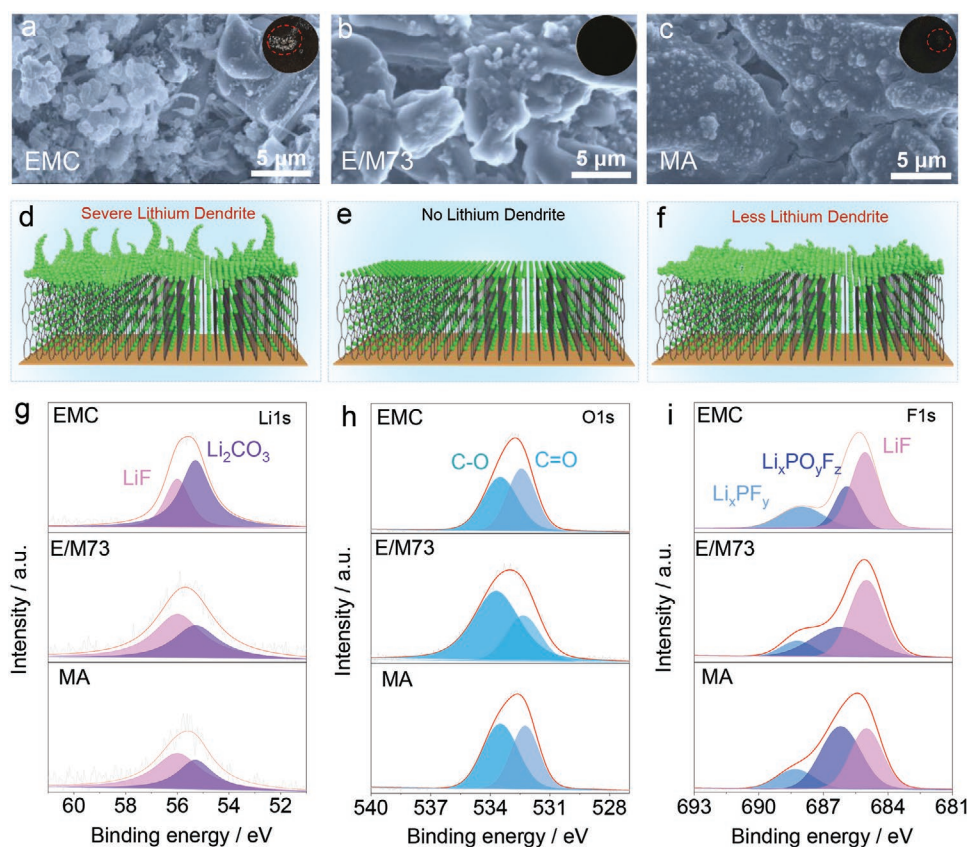


**Figure 4.** Characterizations of graphite anode in the graphite || NCM622 cell employing different electrolytes after 200 cycles. SEM images and illustration of the deposition of lithium metal on cycled graphite electrode in a,d) EMC, b,e) E/M73, and c,f) MA electrolytes. XPS spectra of g) Li 1s, h) O 1s, and i) F 1s of cycled graphite electrode.

(Figure 4g and Figure S7c,d,f, Supporting Information), suggesting an increased formation of  $\text{Li}_2\text{CO}_3$  due to a reaction between the deposited lithium metal and EMC solvent. This is consistent with the result from O 1s spectra judged by C=O at 532.5 eV and the C–O groups at 533.7 eV<sup>[28]</sup> (Figure 4h and Figure S7e, Supporting Information). In addition, the F 1s spectrum of the graphite anode cycled with EMC electrolyte shows a much stronger  $\text{Li}_x\text{PF}_y$  peak (i.e., at 688.3 eV<sup>[33]</sup>) than that of  $\text{Li}_x\text{PO}_y\text{F}_z$  (i.e., at 686.6 eV<sup>[27]</sup>), but the LiF peak (i.e., at 685.0 eV<sup>[35]</sup>) is more obvious in comparison to the MA electrolyte (Figure 4i and Figure S7g, Supporting Information). The result indicates that the decomposition of  $\text{LiPF}_6$ -species is more serious in EMC electrolytes but oxygen-containing organic decomposition products are mainly in the MA electrolytes. The relatively higher content of  $\text{LiCO}_3$  and C–O on the surface of graphite anodes cycled with EMC and MA electrolytes than that with the E/M73 electrolyte further indicates the growth of carbon-oxygen-containing species (Figure S7f, Supporting Information), such as the oligomers formed from the reduction of the electrolyte solvent by the deposited lithium metal. Sets of characterizations on the surface of NCM cathodes and graphite anodes were carried out, which corroborated the roles of the electrolyte composition on the decomposition products. Besides the composition and architecture characterizations of the electrolyte decomposition products, an understanding of the electrolyte decomposition process on the surface of the electrodes

remains unclear, thus, a molecular-scale interfacial model of different electrolyte compositions is needed to interpret the details.

## 2.5. Role of Solvation Structure

The lithium-ion solvation structure first was studied by Fourier Transform infrared spectroscopy (FTIR). The combined peak at 1750 and 1747  $\text{cm}^{-1}$ , corresponding to the C=O stretch vibrations of EMC and MA,<sup>[11,36]</sup> had a redshift and was split into two main peaks at 1718 and 1712  $\text{cm}^{-1}$  when the 1.2 M  $\text{LiPF}_6$  salt was dissolved into the solvent mixture (Figure 5a and Figure S9a, Supporting Information). This is a well-known solvation process, in which the ionic compound of  $\text{Li}^+\text{PF}_6^-$  is solvated by the solvents, and then lithium-ion coordinates with the solvents to form a solvation structure through the  $\text{Li}^+\text{O}$  interactions. Then, the solvated anion ( $\text{PF}_6^-$ ) is classified into uncoordinated (free)  $\text{PF}_6^-$  (at 845  $\text{cm}^{-1}$ ) and  $\text{Li}^+\text{PF}_6^-$  (i.e., contact ion pairs, CIPs) at the peaks of 834 and 870  $\text{cm}^{-1}$ <sup>[37]</sup> (Figure 5b and Figure S9b, Supporting Information). In particular, the coordinated number or proportion of each electrolyte species was quantitatively estimated by deconvoluting the FTIR spectra deliberately (Figure 5e and Table S3, Supporting Information).<sup>[38]</sup>

It was found that the coordination number of MA molecules ( $\text{Li}^+\text{MA}$ ) increased while that of the EMC molecules ( $\text{Li}^+\text{EMC}$ ) and CIPs ratio ( $\text{Li}^+\text{PF}_6^-$ ) decreased with increasing

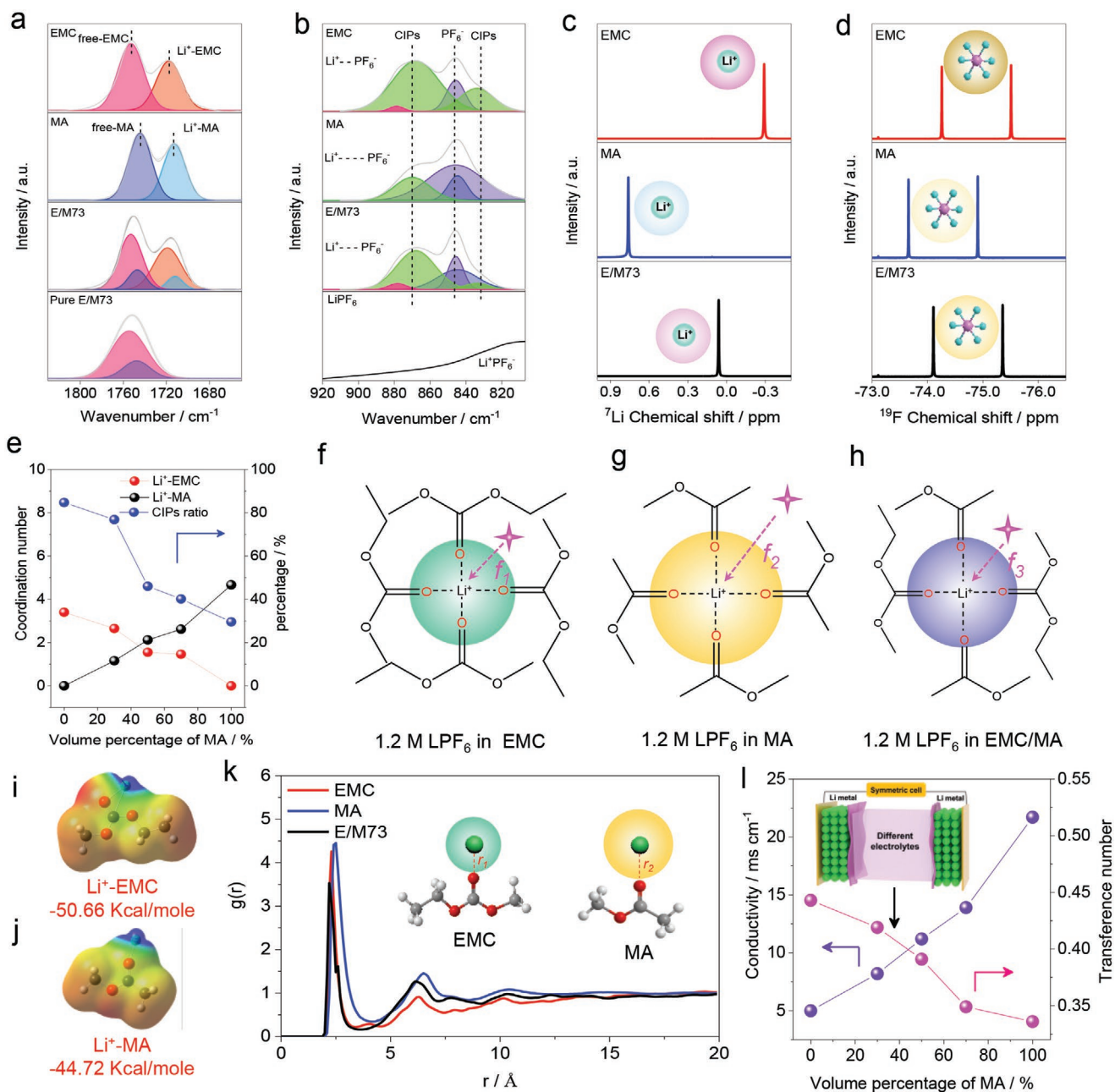


**Figure 5.** Electrolyte analysis and solvation behaviors in different electrolytes. FTIR spectra of a)  $\text{Li}^+$ -solvent, b) free- $\text{PF}_6^-$  or CIPs, c)  $^7\text{Li}$  NMR spectra of  $\text{Li}^+$ , and d)  $^{19}\text{F}$  NMR spectra of  $\text{PF}_6^-$  in different electrolytes. e) Coordination number of  $\text{Li}^+$ -solvent and CIPs ratio obtained from the FTIR fitting results. Frequency of  $\text{PF}_6^-$  contact with the  $\text{Li}^+$  in the f) EMC, g) MA, and h) E/M73 electrolytes. Binding energy of i)  $\text{Li}^+$ -EMC and j)  $\text{Li}^+$ -MA. k) Radial distribution function (RDF) of  $\text{Li}^+$ -O and l) conductivity and transference number of  $\text{Li}^+$  ions in different electrolytes.

volume of MA in the electrolyte. This observation is reasonable because MA has a higher capability to dissociate  $\text{LiPF}_6$  due to its higher dielectric constant (i.e.,  $\epsilon_{\text{MA}} = 6.68$ ) compared to EMC (i.e.,  $\epsilon_{\text{EMC}} = 2.958$ ).<sup>[21]</sup> Thus,  $\text{PF}_6^-$  becomes hard to involve in the  $\text{Li}^+$ -solvation structure when MA is added into the EMC electrolyte, which was further corroborated by the  $^7\text{Li}$  NMR and  $^{19}\text{F}$  NMR analysis of the electrolytes (Figure 5c,d and Figure S9, Supporting Information). First, the  $^7\text{Li}$  NMR chemical shift moved downfield (i.e., to higher values<sup>[39]</sup>) when MA was added into the EMC electrolyte to form E/M73. The

downfield shift appeared because MA participates in the coordination with  $\text{Li}^+$  in the first solvation structure, which reduces the shielding effect on the  $\text{Li}^+$  ions due to the low interaction strength of  $\text{Li}^+$ -MA (i.e.,  $-44.72 \text{ kcal mol}^{-1}$  vs  $-50.66 \text{ kcal mol}^{-1}$  for  $\text{Li}^+$ -EMC) (Figure 5i,j) and reduces the contact opportunity of  $\text{Li}^+$  and  $\text{PF}_6^-$  due to the high dielectric constant of MA. The same phenomenon was observed in the chemical shift of  $^{19}\text{F}$  NMR where MA reduces the shielding effect on the  $\text{Li}^+$  ions and effectively dissociates  $\text{Li}^+$ - $\text{PF}_6^-$  coordination, which is consistent with the observations from FTIR. Based on these

findings, the proposed coordination structures are illustrated in Figure 5f–h.

Note that the above analysis presented in Figure 5a–h is an average coordination structure for  $\text{Li}^+$  and the solvent, while one  $\text{Li}^+$  can coordinate with four solvent molecules in the electrolyte. EMC has a strong interaction with  $\text{Li}^+$  in the solvation structure in the EMC electrolyte, and  $\text{PF}_6^-$  may contact with  $\text{Li}^+$  in a high frequency due to the low dielectric constant, as demonstrated by the high CIP ratio (i.e.,  $\text{Li}^+\text{-PF}_6^-$ ) in FTIR (Figure 5f–h). In contrast, MA has a relatively weak interaction (vs EMC) with  $\text{Li}^+$  in the solvation structure, and  $\text{PF}_6^-$  is hard to contact with  $\text{Li}^+$  because of the high dielectric constant. Then, the appearance frequency of  $\text{PF}_6^-$  around the first solvation structure in the electrolyte decreases in the sequence  $\text{EMC} > \text{E/M73} > \text{MA}$  (i.e.,  $f_1 > f_3 > f_2$ ).

The  $\text{Li}^+\text{-O}$  radial distribution function (RDF) corroborated the different interactions between the solvents (e.g., EMC and MA) and  $\text{Li}^+$  (Figure 5k). The  $\text{Li}^+\text{-EMC}$  coordination is stronger than that of  $\text{Li}^+\text{-MA}$ , which is consistent with the observed strong shielding effect and the chemical shift that appeared at high-field in the NMR spectrum (Figure 5c). The  $\text{Li}^+\text{-PF}_6^-$  NMR for the  $\text{PF}_6^-$  neighbor to  $\text{Li}^+$  also confirmed the higher frequency of  $\text{PF}_6^-$  appearing around  $\text{Li}^+$  in the EMC electrolyte than that in the MA electrolyte (Figure 5d). In brief, the MA solvent can dissociate  $\text{LiPF}_6$  effectively and compete with the EMC solvent to participate in the first solvation structure around  $\text{Li}^+$  when MA is added into the EMC electrolyte. Then,  $\text{PF}_6^-$  is easy to contact with  $\text{Li}^+$  and form CIPs in EMC electrolytes (EMC and E/M73), but  $\text{PF}_6^-$  can be excluded from the solvation structure by MA in the MA electrolyte. These results are consistent with the FTIR and NMR results.

As a result, the conductivity of the electrolyte increased from 5.0 to 21.7  $\text{mS cm}^{-1}$  with increasing the amount of MA from 0% to 100% (Figure 5l). This is because EMC could be replaced by MA in the solvation structure, where  $\text{PF}_6^-$  could also keep far from  $\text{Li}^+$  due to the higher dissociated capability and then demonstrate enhanced mobility. In contrast, the transference number of  $\text{Li}^+$  decreases from 0.443 to 0.336 with increasing the amount of MA, especially when the percentage volume of MA is more than 50%. This is consistent with the increased mobility of  $\text{PF}_6^-$  (i.e.,  $t_+ + t_- = 1$ ) (Figure 5l; the calculation of  $t_{\text{Li}^+}$  resulted from Figure S10, Supporting Information).<sup>[40]</sup> These results are in good agreement with the change of CIPs ratio, in which the presence of  $\text{PF}_6^-$  was excluded from the solvation structure (i.e., the increased number of free  $\text{PF}_6^-$ ). Note that although there is a high transference number in the EMC electrolyte, the very low conductivity of 5.0  $\text{mS cm}^{-1}$  could cause lithium metal deposition on the graphite anode due to severe concentration polarization (Figure 4a,d). The E/M73 electrolyte has a suitable conductivity of 8.2  $\text{mS cm}^{-1}$  and a transference number of 0.419, which guarantees a good rate capability and lithium-dendrite-free fast charging features (Figures 1e,f and 4b,e).

## 2.6. Simulation of Electrolyte Behavior

The  $\text{Li}^+$ -solvation structure in the bulk electrolyte was investigated to interpret the observed electrochemical performance in

different electrolytes. Then, a solvation structure-related interfacial model can be constructed to interpret the root cause of the varied performance in the different electrolytes. First, the electron distribution of the  $\text{Li}^+\text{-solvent-PF}_6^-$  complexes (i.e., CIPs) illustrated by electrostatic potential mapping was developed (presented in Figure 6a). The active electrons of the  $\text{Li}^+\text{-solvent-PF}_6^-$  complexes increase with the increasing volume of MA solvent. This finding demonstrates that a high Coulombic interaction exists between  $\text{PF}_6^-$  and the positively charged cathode electrode when the volume of MA solvent is dominant in the electrolyte (e.g., the volume of MA > 50%). Second, the desolvation energy of  $\text{Li}^+$  was also considered to analyze the interaction between the  $\text{Li}^+\text{-solvent-PF}_6^-$  in different electrolytes (Figure 6b). It was found that the  $\text{Li}^+$  desolvation energy ( $E_{\text{Li}^+}^{\text{-3MA-PF}_6^-}$ ,  $-84.9 \text{ kcal mol}^{-1}$ ,  $E_{\text{Li}^+}^{\text{-2MA-EMC-PF}_6^-}$ ,  $-92.41 \text{ kcal mol}^{-1}$ , or  $E_{\text{Li}^+}^{\text{-MA-2EMC-PF}_6^-}$ ,  $-97.39 \text{ kcal mol}^{-1}$ ) was reduced when the volume of MA solvent was dominant in electrolyte compared to that of EMC ( $E_{\text{Li}^+}^{\text{-3EMC-PF}_6^-}$ ,  $-101.34 \text{ kcal mol}^{-1}$ ). This implies that the  $\text{Li}^+\text{-solvent-anion}$  complexes interaction is much weaker in the presence of MA and E/M73 than that in EMC electrolyte, which could affect the Li deposition or  $\text{Li}^+$  (de)-intercalation behavior at graphite.

The HOMO and LUMO energy of the solvent, solvent- $\text{PF}_6^-$ ,  $\text{Li}^+\text{-solvent}$ , and  $\text{Li}^+\text{-solvent-PF}_6^-$  complex are presented in Figure 6c. It was found that the oxidation stability of all solvents increased when the solvent coordinated to  $\text{Li}^+$  (i.e., the HOMO energy of  $\text{Li}^+\text{-solvent}$  is lower than solvent), but the stability was weakened once the solvent coordinated with  $\text{PF}_6^-$  (i.e., the HOMO energy of solvent- $\text{PF}_6^-$  is higher than solvent, or  $\text{Li}^+\text{-solvent-PF}_6^-$  is higher than  $\text{Li}^+\text{-solvent}$ ). This is because the solvent-induced by  $\text{PF}_6^-$  can lose electrons more easily, and then the H-abstraction of solvent can occur at high potential, forming HF upon cycling. Thus, making  $\text{PF}_6^-$  away from the solvent is important to maintain electrolyte stability at the cathode interface, while the reduced ability of solvent,  $\text{Li}^+\text{-solvent}$ , and  $\text{Li}^+\text{-solvent-PF}_6^-$  must also be considered.

## 2.7. Interfacial Model

The electrolyte formula of  $\text{Li}^+[\text{solvent}]_x[\text{PF}_6^-]$  ( $x$ , calculated using the molar concentration) was used to describe the electrolyte-electrode interfacial behaviors.<sup>[41]</sup> For example, 1.2 M  $\text{LiPF}_6$  solvation in the EMC, E/M73, and MA electrolytes are described as  $\text{Li}^+[\text{EMC}]_{8.11}[\text{PF}_6^-]$ ,  $\text{Li}^+[\text{MA}]_{3.14}[\text{EMC}]_{5.68}[\text{PF}_6^-]$  and  $\text{Li}^+[\text{MA}]_{10.46}[\text{PF}_6^-]$ , respectively. Then, the interfacial model was derived when  $\text{Li}^+$  was de-solvated from the solvation structure. The relative frequency of  $\text{PF}_6^-$  around the  $\text{Li}^+$  solvation structure in the bulk electrolytes and at the electrolyte-electrode interfaces is presented in Figure 7. Different interfacial behaviors of the electrolytes and their relations with the electrode performances are discussed in detail later.

In the EMC electrolyte,  $\text{PF}_6^-$  appears around  $\text{Li}^+$  in the solvation structure with a high frequency (i.e.,  $f_1$ ) due to the low dielectric constant of EMC (i.e., the high CIPs ratio) in the EMC electrolyte. A strong interaction (i.e.,  $f_1'$ ) exists between  $\text{Li}^+$  and  $\text{EMC-PF}_6^-$ , and such an interaction weakens the Coulombic interaction between  $\text{PF}_6^-$  and the positively charged cathode (Figure 7a). In this state, the  $\text{EMC-PF}_6^-$  pair is difficult



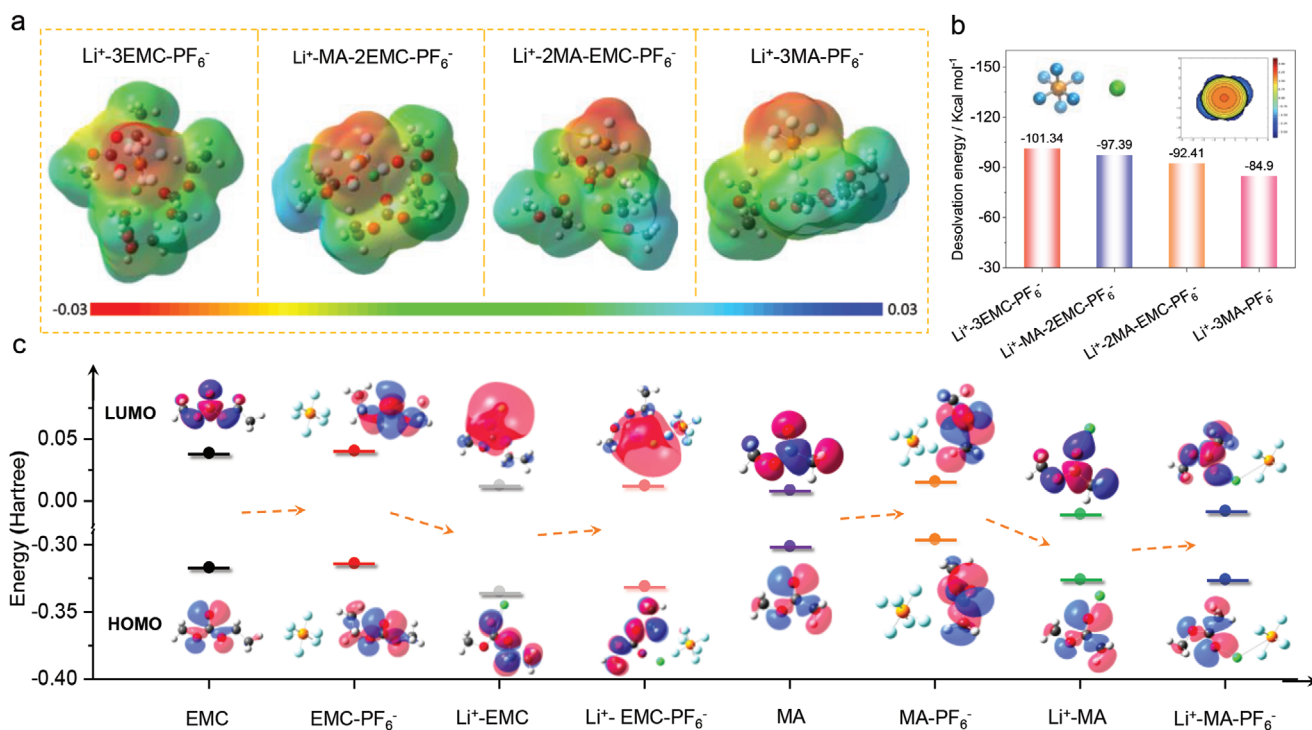


**Figure 6.** Simulated solvation behaviors in different solvents. a) Electrostatic potential mapping about electron distribution for different Li<sup>+</sup>-solvent-PF<sub>6</sub><sup>-</sup> pair. b) Desolvation energies between Li<sup>+</sup>-solvents-PF<sub>6</sub><sup>-</sup> obtained by DFT calculations (right inset is the simulation snapshot of Buried volume [%V<sub>Bur</sub>] calculations for PF<sub>6</sub><sup>-</sup>). c) LUMO and HOMO energy of the solvent, solvent-PF<sub>6</sub><sup>-</sup>, Li<sup>+</sup>-solvent, and Li<sup>+</sup>-solvent-PF<sub>6</sub><sup>-</sup> pair (insets are molecular orbital simulation snapshots of LUMO and HOMO).

to move closer toward the surface of the cathode due to the weak interaction. As a result, EMC-PF<sub>6</sub><sup>-</sup> is also hard to oxidize due to the difficulty in transferring electrons to the cathode and the high oxidation stability (vs MA-PF<sub>6</sub><sup>-</sup>). Besides, the oxidation stability of free EMC solvent is also improved, because the free EMC coordinates with Li<sup>+</sup> when Li<sup>+</sup> is extracted from the cathode upon the charging process to form the Li<sup>+</sup>-EMC pair (i.e., the HOMO energy of Li<sup>+</sup>-EMC was lower than free EMC) (Figure 6c). In particular, PF<sub>6</sub><sup>-</sup> is also difficult to de-solvate in the initial Li<sup>+</sup> solvation structure and then moves closer to the newly formed Li<sup>+</sup>-EMC pair (i.e., the less free PF<sub>6</sub><sup>-</sup> can move close to the Li<sup>+</sup>-EMC pair as most of PF<sub>6</sub><sup>-</sup> bounds to around Li<sup>+</sup> and solvent in the bulk electrolyte due to the high CIPs ratio). Thus, the detrimental effect of the PF<sub>6</sub><sup>-</sup> reaction with EMC solvent that produces HF could be effectively mitigated. In this EMC electrolyte system, EMC-PF<sub>6</sub><sup>-</sup> and EMC could be well-stabilized even at a high charge voltage condition; however, the low ionic conductivity of the EMC electrolyte gives rise to a low-rate capacity (Figure 1e,f).

In contrast, the solvation structure in the MA electrolyte shows PF<sub>6</sub><sup>-</sup> with a low frequency that appears around Li<sup>+</sup> (i.e.,  $f_2$ ) in the solvation structure due to the high dielectric constant of MA (i.e., the low CIPs ratio) in the MA electrolyte (Figure 7b). Thus, the MA-PF<sub>6</sub><sup>-</sup> pair demonstrates a weak interaction with Li<sup>+</sup> (i.e.,  $f_2'$ ), then the MA-PF<sub>6</sub><sup>-</sup> can move closer to the cathode surface due to the strong Coulombic interaction between PF<sub>6</sub><sup>-</sup> and the positively charged cathode. As a result, electron transfer from MA-PF<sub>6</sub><sup>-</sup> to the cathode is possible, leading to a lower oxidation stability of MA-PF<sub>6</sub><sup>-</sup> compared to that of

EMC-PF<sub>6</sub><sup>-</sup>. Note that the oxidation stability of the free MA solvent is not improved, as the case is opposite in the EMC electrolyte, because PF<sub>6</sub><sup>-</sup> can be de-solvated from the initial Li<sup>+</sup> solvation structure readily and then moves closer toward the newly formed Li<sup>+</sup>-MA pair. The free PF<sub>6</sub><sup>-</sup> can move closer toward the formed Li<sup>+</sup>-MA as most of PF<sub>6</sub><sup>-</sup> is not bound with Li<sup>+</sup> and solvents in the bulk electrolyte (i.e., the low CIPs ratio), when Li<sup>+</sup> was extracted from the cathode. As a result, PF<sub>6</sub><sup>-</sup> promotes the oxidation of Li<sup>+</sup>-MA more easily on the cathode surface, as judged by the HOMO of Li<sup>+</sup>-MA and Li<sup>+</sup>-MA-PF<sub>6</sub><sup>-</sup> (Figure 6c), leading to a severe decomposition of the MA electrolyte on the cathode surface.

In the E/M73 electrolyte, MA solvent participates in the first solvation structure, where partial MA can involve in the dissociation of Li<sup>+</sup>-PF<sub>6</sub><sup>-</sup> because of insufficient EMC (i.e., Li<sup>+</sup>[MA]<sub>3,14</sub>[EMC]<sub>5,68</sub>[PF<sub>6</sub><sup>-</sup>]). This analysis is consistent with the observed medium CIPs ratio in the E/M73 electrolyte. PF<sub>6</sub><sup>-</sup> has a medium frequency (i.e.,  $f_3$ ) that appeared around Li<sup>+</sup>, the value of which is lower than that in the EMC electrolyte (i.e.,  $f_1 > f_3$ ) but higher than that in the MA electrolyte (i.e.,  $f_3 > f_2$ ) (Figure 5f-h). Then, PF<sub>6</sub><sup>-</sup> demonstrates a medium interaction with the Li<sup>+</sup>-solvent in the E/M73 electrolyte compared to those in the EMC and MA electrolytes (i.e.,  $f_1' > f_3' > f_2'$ ), giving rise to a medium Coulombic interaction and a safe distance between the PF<sub>6</sub><sup>-</sup> and the positively charged cathode (Figure 7c). As a result, the MA-PF<sub>6</sub><sup>-</sup> pair is hard to oxidize due to the difficulty in transferring electrons to the cathode and also its high oxidation stability (i.e., MA is close to Li<sup>+</sup> but far from PF<sub>6</sub><sup>-</sup>). This phenomenon is similar to that in the

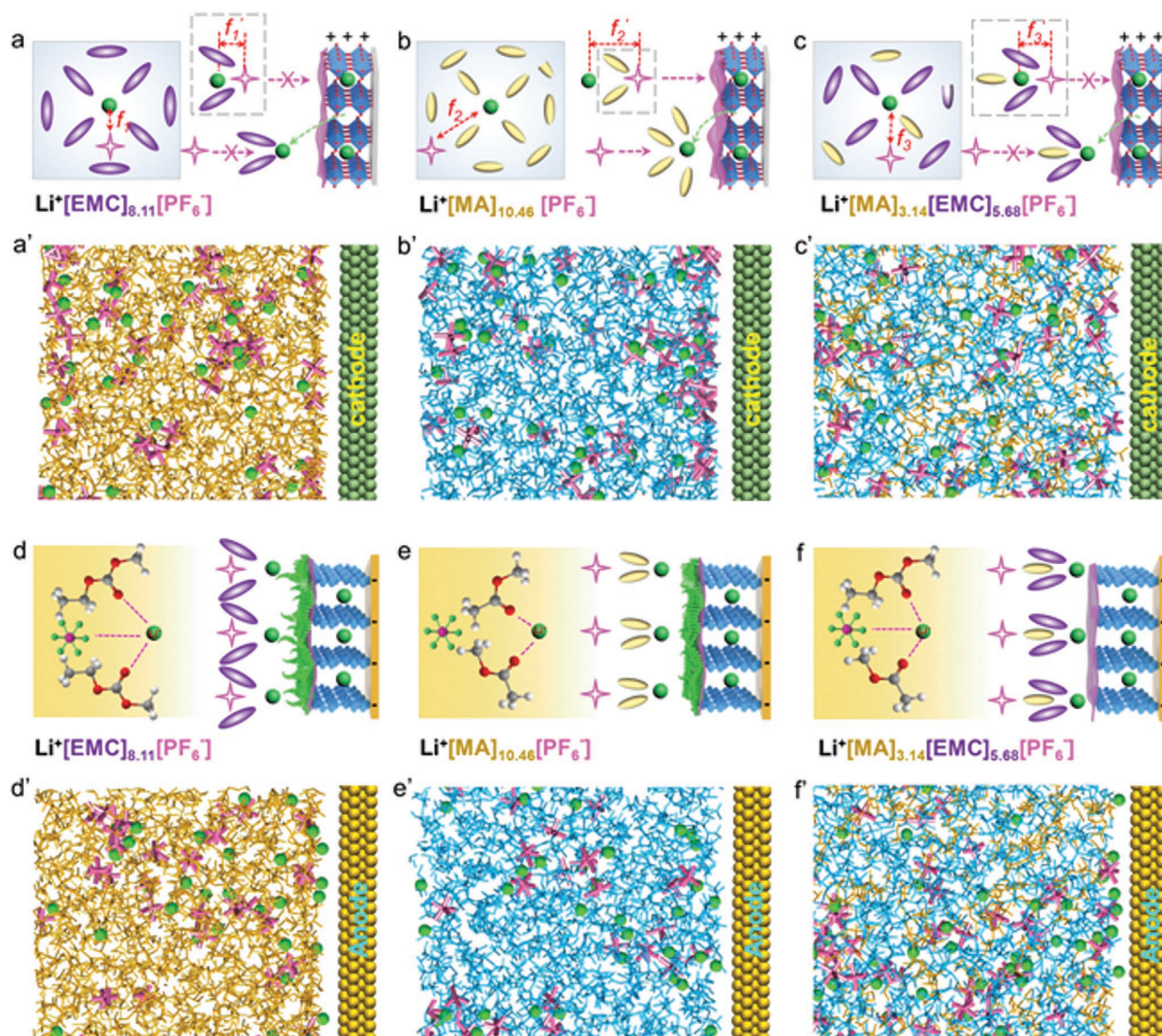


**Figure 7.** Interfacial behavior and simulation from the bulk electrolyte to electrode interphase. a–c) Cathode interfacial model and a'–c') simulated electrolyte behavior on the cathode/electrolyte interphase, d–f) anode interfacial model, and d'–f') simulated electrolyte behavior on the anode/electrolyte interphase in the EMC, MA, and E/M73 electrolytes, respectively.

EMC electrolyte. Moreover, the EMC solvent can also prevent  $\text{PF}_6^-$  moving closer to the  $\text{Li}^+$ –MA pair at the surface of the cathode when  $\text{Li}^+$  is extracted from the cathode. This conjecture was further corroborated by the simulations, where the frequency of  $\text{PF}_6^-$  appeared around the surface of the cathode in the sequence EMC < E/M73 < MA electrolytes (Figure 7a'–c'). These results demonstrate the importance of solvent to determine the stability of electrolytes on the surface of the cathode at high potential.

Our interfacial model was also well-constructed on the surface of the graphite anode. In the EMC electrolyte,  $\text{Li}^+$  could interact with  $\text{PF}_6^-$  via strong binding energy and high frequency (i.e.,  $f_1$ ) due to the low dielectric constant of EMC (Figure 5f), giving rise to high de-solvation energy (Figure 6b). Thus, lithium dendrite is easy to plate on the graphite anode

because of the resultant high polarization. This process is detrimental because lithium can react with the EMC solvent due to the lower reduction stability of the  $\text{Li}^+$ –EMC pair.<sup>[42]</sup> This finding not only interprets the observed lithium on the graphite anode in Figure 4a but also explains the root cause of the reduced cycling stability of the battery in the EMC electrolyte (Figure S3b, Supporting Information). Note that some side-reaction products can be observed in the MA electrolyte resulting in the lower formation of lithium dendrite, which is attributed to a low  $\text{Li}^+$  de-solvation energy (Figure 6b) and the side-effects of the polarization are less than that in the EMC electrolyte (a weaker interaction between  $\text{Li}^+$  and MA solvent or anion in Figure 5g,j). On the other hand, the side-reaction between lithium dendrite and MA is a serious issue, occurring because the LUMO energy of MA electrolyte is low (Figure 6c).



Thus, decomposition products of the electrolyte are observed at the graphite anode. This finding further demonstrates that although the single MA solvent can regulate the intercalation or deposition of  $\text{Li}^+$  by reducing the polarization, the high reduction activity would lead to the decay of the battery.

Interestingly, a completely different interfacial behavior was found in the E/M73 electrolyte. First, the interaction between EMC and  $\text{Li}^+$  is weakened by the MA solvent, where  $\text{PF}_6^-$  could also keep far from  $\text{Li}^+$  compared to the situation in the EMC electrolyte. Then,  $\text{Li}^+$  de-solvation becomes easier, under which the intercalation of  $\text{Li}^+$  into graphite anode is preferable compared to the formation of lithium dendrite. Moreover, the reduction stability of E/M73 could be improved further because the EMC solvent can compete with MA in the  $\text{Li}^+$  solvation structure. Thus, the E/M73 electrolyte has the combined advantages of EMC and MA electrolytes, thereby demonstrating better stability without the formation of lithium dendrite and enabling a good cycling performance of the battery. Note that this conjecture was further corroborated by the simulations, where the MA solvent could change the interfacial behaviors (i.e.,  $\text{Li}^+$ -solvent-anion interactions) when the MA was added into EMC electrolyte for form E/M73 (Figure 7d'-f').

To this end, we have not only built a new interfacial model on the cathode side for the first time, but also constructed the dynamic mutual-interaction interfacial behavior on the cathode and anode simultaneously to interpret the battery performance. The varied electrolyte-electrode behaviors (i.e., the behaviors of  $\text{Li}^+$ -solvent-anion pairs) were thoroughly studied by experiments (e.g., FTIR and NMR) and simulations, which enable us to unravel the relationship between the interfacial behaviors and the electrode performance. This breakthrough could advance the development of battery electrolytes. To date, numerous simulations have been devoted to exploring the properties of electrolytes, which covers the study of stability and decomposition routines of electrolytes, as well as variation in the  $\text{Li}^+$  solvation structure from bulk electrolytes to electrode interfaces.<sup>[43]</sup> However, to the best of our knowledge, there is no report to date on interfacial models that elucidate the relationships between interfacial behavior and the electrode performance. Based on our results, we believe that the interfacial interaction is a significant factor that affects the battery performance, of which at least the interfacial interactions are similarly important to the role of SEI/CEI.<sup>[14c,44]</sup> Our discovery provides a new viewpoint for understanding the electrolyte-electrode interactions and then efficiently improving the battery performance, prompting the development of future batteries with diverse systems. Therefore, the development of knowledge about the effects of SEI/CEI and electrolyte-electrode interfacial interactions (i.e., the behaviors of the  $\text{Li}^+$ -solvent-anion pair) should be kept in balance simultaneously when designing future electrolytes.

### 3. Conclusion

A new high-voltage electrolyte employing a cosolvent strategy without any additive has been demonstrated, showing a fast-charging capability of LIBs with an excellent long-term cycle performance, high-power stability, and lithium-dendrite free

electrodes. More importantly, a pioneering interfacial model related to the  $\text{Li}^+$  solvation structure has been presented, both on the cathode and anode, which unravels the molecular-scale of  $\text{Li}^+$ -solvent-anion interactions on the surface of the electrodes as well as their roles in battery performance. The interfacial model elucidates a new viewpoint to understand the key relationships between  $\text{Li}^+$  solvation structure in the electrolyte and the performance of electrodes, paving the way to hitherto undiscovered guidelines for designing electrolytes for metal-ion batteries.

### Supporting Information

Supporting Information is available from the Wiley Online Library or from the author.

### Acknowledgements

Y.Z. and Z.C. contributed equally to this work. This work was supported by the National Natural Science Foundation of China (22122904, 21978281, 21975250, and 11974150) and the National Key R&D Program of China (2017YFE0198100). The authors also wish to thank the Independent Research Project of the State Key Laboratory of Rare Earth Resources Utilization (110005R086), Changchun Institute of Applied Chemistry, Chinese Academy of Sciences. The research was also supported by King Abdullah University of Science and Technology (KAUST) and Hanyang University. The computational work was done on the KAUST supercomputer.

### Conflict of Interest

The authors declare no conflict of interest.

### Data Availability Statement

Research data are not shared.

### Keywords

electrolyte-electrode interfaces, fast charging high-voltage electrolytes, lithium-ion batteries, solvation structures

Received: April 19, 2021  
Revised: August 5, 2021  
Published online: September 12, 2021

- [1] a) J. M. Tarascon, M. Armand, *Nature* **2001**, *414*, 359; b) B. Scrosati, J. Hassoun, Y.-K. Sun, *Energy Environ. Sci.* **2011**, *4*, 3287; c) M. Li, J. Lu, Z. Chen, K. Amine, *Adv. Mater.* **2018**, *30*, 1800561.  
[2] a) Y. Q. Wu, W. X. Wang, J. Ming, M. L. Li, L. Q. Xie, X. M. He, J. Wang, S. Q. Liang, Y. P. Wu, *Adv. Funct. Mater.* **2019**, *29*, 1805978; b) E. R. Logan, J. R. Dahn, *Trends Chem.* **2020**, *2*, 354; c) X. D. Lin, G. D. Zhou, J. P. Liu, J. Yu, M. B. Effat, J. X. Wu, F. Ciucci, *Adv. Energy Mater.* **2020**, *10*, 2001235.  
[3] a) Y. K. Sun, S. T. Myung, B. C. Park, J. Prakash, I. Belharouak, K. Amine, *Nat. Mater.* **2009**, *8*, 320; b) Y. K. Sun, Z. Chen, H. J. Noh,



- D. J. Lee, H. G. Jung, Y. Ren, S. Wang, C. S. Yoon, S. T. Myung, K. Amine, *Nat. Mater.* **2012**, *11*, 942; c) A. Manthiram, J. C. Knight, S.-T. Myung, S.-M. Oh, Y.-K. Sun, *Adv. Energy Mater.* **2016**, *6*, 1501010.
- [4] a) J. Ma, P. Hu, G. Cui, L. Chen, *Chem. Mater.* **2016**, *28*, 3578; b) G. Xu, C. Pang, B. Chen, J. Ma, X. Wang, J. Chai, Q. Wang, W. An, X. Zhou, G. Cui, L. Chen, *Adv. Energy Mater.* **2018**, *8*, 1701398; c) Y. Ma, K. Chen, J. Ma, G. Xu, S. Dong, B. Chen, J. Li, Z. Chen, X. Zhou, G. Cui, *Energy Environ. Sci.* **2019**, *12*, 273.
- [5] a) S. Ye, L. Wang, F. Liu, P. Shi, H. Wang, X. Wu, Y. Yu, *Adv. Energy Mater.* **2020**, *10*, 2002647; b) H. Zheng, H. Xiang, F. Jiang, Y. Liu, Y. Sun, X. Liang, Y. Feng, Y. Yu, *Adv. Energy Mater.* **2020**, *10*, 2001440; c) Q. Li, Z. Cao, G. Liu, H. Cheng, Y. Wu, H. Ming, G. T. Park, D. Yin, L. Wang, L. Cavallo, Y. K. Sun, J. Ming, *J. Phys. Chem. Lett.* **2021**, *12*, 4857.
- [6] H. Xue, Y. Wu, Y. Zou, Y. Shen, G. Liu, Q. Li, D. Yin, L. Wang, J. Ming, *Adv. Funct. Mater.* **2020**, *30*, 1910657.
- [7] a) L. Zhou, J. Zhang, Y. Q. Wu, W. X. Wang, H. Ming, Q. J. Sun, L. M. Wang, J. Ming, H. N. Alshareef, *Adv. Energy Mater.* **2019**, *9*, 1902194; b) L. Zhou, Z. Cao, W. Wahyudi, J. Zhang, J.-Y. Hwang, Y. Cheng, L. Wang, L. Cavallo, T. Anthopoulos, Y.-K. Sun, H. N. Alshareef, J. Ming, *ACS Energy Lett.* **2020**, *5*, 766.
- [8] a) J. Ming, Z. Cao, W. Wahyudi, M. Li, P. Kumar, Y. Wu, J.-Y. Hwang, M. N. Hedhili, L. Cavallo, Y.-K. Sun, L.-J. Li, *ACS Energy Lett.* **2018**, *3*, 335; b) J. Ming, Z. Cao, Y. Wu, W. Wahyudi, W. Wang, X. Guo, L. Cavallo, J.-Y. Hwang, A. Shamim, L.-J. Li, Y.-K. Sun, H. N. Alshareef, *ACS Energy Lett.* **2019**, *4*, 2613; c) J. Ming, Z. Cao, Q. Li, W. Wahyudi, W. Wang, L. Cavallo, K.-J. Park, Y.-K. Sun, H. N. Alshareef, *ACS Energy Lett.* **2019**, *4*, 1584.
- [9] a) S. Zhang, J. Ma, Z. Hu, G. Cui, L. Chen, *Chem. Mater.* **2019**, *31*, 6033; b) G. Xu, X. Shangguan, S. Dong, X. Zhou, G. Cui, *Angew. Chem., Int. Ed.* **2020**, *59*, 3400.
- [10] Y. Zou, Y. Shen, Y. Wu, H. Xue, Y. Guo, G. Liu, L. Wang, J. Ming, *Chem. - Eur. J.* **2020**, *26*, 7930.
- [11] Y. R. Zhang, Y. Katayama, R. Tataru, L. Giordano, Y. Yu, D. Fraggedakis, J. G. W. Sun, F. Maglia, R. Jung, M. Z. Bazant, Y. Shao-Horn, *Energy Environ. Sci.* **2020**, *13*, 183.
- [12] A. T. S. Freiberg, M. K. Roos, J. Wandt, R. de Vivie-Riedle, H. A. Gasteiger, *J. Phys. Chem. A* **2018**, *122*, 8828.
- [13] A. Tornheim, S. Sharifi-Asl, J. C. Garcia, J. Bareno, H. Iddir, R. Shahbazian-Yassar, Z. C. Zhang, *Nano Energy* **2019**, *55*, 216.
- [14] a) J. Alvarado, M. A. Schroeder, M. H. Zhang, O. Borodin, E. Gobrogge, M. Olguin, M. S. Ding, M. Gobet, S. Greenbaum, Y. S. Meng, K. Xu, *Mater. Today* **2018**, *21*, 341; b) J. Fu, X. Ji, J. Chen, L. Chen, X. Fan, D. Mu, C. Wang, *Angew. Chem., Int. Ed.* **2020**, *59*, 22194; c) S. Liu, X. Ji, N. Piao, J. Chen, N. Eidson, J. Xu, P. Wang, L. Chen, J. Zhang, T. Deng, S. Hou, T. Jin, H. Wan, J. Li, J. Tu, C. Wang, *Angew. Chem., Int. Ed.* **2021**, *60*, 3661.
- [15] S. Chen, J. Zheng, D. Mei, K. S. Han, M. H. Engelhard, W. Zhao, W. Xu, J. Liu, J. G. Zhang, *Adv. Mater.* **2018**, *30*, 1706102.
- [16] M. N. He, C. C. Su, Z. X. Feng, L. Zeng, T. P. Wu, M. J. Bedzyk, P. Fenter, Y. Wang, Z. C. Zhang, *Adv. Energy Mater.* **2017**, *7*, 1700109.
- [17] a) J. Xia, M. Nie, J. Burns, A. Xiaow, W. Lamanna, J. Dahn, *J. Power Sources* **2016**, *307*, 340; b) J. Xia, K. J. Nelson, Z. H. Lu, J. R. Dahn, *J. Power Sources* **2016**, *329*, 387.
- [18] a) Q. Q. Liu, D. J. Xiong, R. Petibon, C. Y. Du, J. R. Dahn, *J. Electrochem. Soc.* **2016**, *163*, A3010; b) Q. Q. Liu, R. Petibon, C. Y. Du, J. R. Dahn, *J. Electrochem. Soc.* **2017**, *164*, A1173.
- [19] L. Ma, S. L. Glazier, R. Petibon, J. Xia, J. M. Peters, Q. Liu, J. Allen, R. N. C. Doig, J. R. Dahn, *J. Electrochem. Soc.* **2016**, *164*, A5008.
- [20] E. R. Logan, D. S. Hall, M. M. E. Cormier, T. Taskovic, M. Bauer, I. Hamam, H. Hebecker, L. Molino, J. R. Dahn, *J. Phys. Chem. C* **2020**, *124*, 12269.
- [21] E. R. Logan, E. M. Tonita, K. L. Gering, J. Li, X. W. Ma, L. Y. Beaulieu, J. R. Dahn, *J. Electrochem. Soc.* **2018**, *165*, A21.
- [22] G. A. Elia, U. Ulissi, S. Jeong, S. Passerini, J. Hassoun, *Energy Environ. Sci.* **2016**, *9*, 3210.
- [23] T. R. Tanim, M. G. Shirk, R. L. Bewley, E. J. Dufek, B. Y. Liaw, *J. Power Sources* **2018**, *381*, 56.
- [24] G. Xu, S. Huang, Z. Cui, X. Du, X. Wang, D. Lu, X. Shangguan, J. Ma, P. Han, X. Zhou, G. Cui, *J. Power Sources* **2019**, *416*, 29.
- [25] a) B. B. Lim, S. J. Yoon, K. J. Park, C. S. Yoon, S. J. Kim, J. J. Lee, Y. K. Sun, *Adv. Funct. Mater.* **2015**, *25*, 4673; b) G. Xu, L. Huang, C. Lu, X. Zhou, G. Cui, *Energy Storage Mater.* **2020**, *31*, 72.
- [26] Y. Wu, M. Li, W. Wahyudi, G. Sheng, X. Miao, T. D. Anthopoulos, K.-W. Huang, Y. Li, Z. Lai, *ACS Omega* **2019**, *4*, 13972.
- [27] S. Verdier, L. El Ouatani, R. Dedryvère, F. Bonhomme, P. Biensan, D. Gonbeau, *J. Electrochem. Soc.* **2007**, *154*, A1088.
- [28] W. Zhao, J. Zheng, L. Zou, H. Jia, B. Liu, H. Wang, M. H. Engelhard, C. Wang, W. Xu, Y. Yang, J.-G. Zhang, *Adv. Energy Mater.* **2018**, *8*, 1800297.
- [29] Y. Yu, P. Karayalali, Y. Katayama, L. Giordano, M. Gauthier, F. Maglia, R. Jung, I. Lund, Y. Shao-Horn, *J. Phys. Chem. C* **2018**, *122*, 27368.
- [30] Y. Q. Wu, H. Ming, M. L. Li, J. L. Zhang, W. Wahyudi, L. Q. Xie, X. M. He, J. Wang, Y. P. Wu, J. Ming, *ACS Energy Lett.* **2019**, *4*, 656.
- [31] S. H. Song, M. Cho, I. Park, J. G. Yoo, K. T. Ko, J. Hong, J. Kim, S. K. Jung, M. Avdeev, S. Ji, S. Lee, J. Bang, H. Kim, *Adv. Energy Mater.* **2020**, *10*, 2000521.
- [32] K. Kim, H. Ma, S. Park, N.-S. Choi, *ACS Energy Lett.* **2020**, *5*, 1537.
- [33] X. H. Zhang, L. F. Zou, Y. B. Xu, X. Cao, M. H. Engelhard, B. E. Matthews, L. R. Zhong, H. P. Wu, H. Jia, X. D. Ren, P. Y. Gao, Z. H. Chen, Y. Qin, C. Kompella, B. W. Arey, J. Li, D. Y. Wang, C. M. Wang, J. G. Zhang, W. Xu, *Adv. Energy Mater.* **2020**, *10*, 2000368.
- [34] X. Shangguan, G. Xu, Z. Cui, Q. Wang, X. Du, K. Chen, S. Huang, G. Jia, F. Li, X. Wang, D. Lu, S. Dong, G. Cui, *Small* **2019**, *15*, 1900269.
- [35] Q. Zheng, Y. Yamada, R. Shang, S. Ko, Y.-Y. Lee, K. Kim, E. Nakamura, A. Yamada, *Nat. Energy* **2020**, *5*, 291.
- [36] L. Zhang, H. Y. Wang, *J. Electrochem. Soc.* **2020**, *167*, 100506.
- [37] A. V. Cresce, S. M. Russell, O. Borodin, J. A. Allen, M. A. Schroeder, M. Dai, J. Peng, M. P. Gobet, S. G. Greenbaum, R. E. Rogers, K. Xu, *Phys. Chem. Chem. Phys.* **2016**, *19*, 574.
- [38] N. Chapman, O. Borodin, T. Yoon, C. C. Nguyen, B. L. Lucht, *J. Phys. Chem. C* **2017**, *121*, 2135.
- [39] W. Zhang, Q. Wu, J. Huang, L. Fan, Z. Shen, Y. He, Q. Feng, G. Zhu, Y. Lu, *Adv. Mater.* **2020**, *32*, 2001740.
- [40] a) W. Fan, N. W. Li, X. Zhang, S. Zhao, R. Cao, Y. Yin, Y. Xing, J. Wang, Y. G. Guo, C. Li, *Adv. Sci.* **2018**, *5*, 1800559; b) S. Wei, S. Inoue, D. Di Lecce, Z. Li, Y. Tominaga, J. Hassoun, *ChemElectroChem* **2020**, *7*, 2376; c) J. Popovic, G. Hasegawa, I. Moudrakovski, J. Maier, *J. Mater. Chem. A* **2016**, *4*, 7135.
- [41] a) G. Liu, Z. Cao, L. Zhou, J. Zhang, Q. Sun, J. Y. Hwang, L. Cavallo, L. Wang, Y. K. Sun, J. Ming, *Adv. Funct. Mater.* **2020**, *30*, 2001934; b) J. Zhang, Z. Cao, L. Zhou, G. Liu, G.-T. Park, L. Cavallo, L. Wang, H. N. Alshareef, Y.-K. Sun, J. Ming, *ACS Energy Lett.* **2020**, *5*, 2651; c) L. Zhou, Z. Cao, J. Zhang, H. Cheng, G. Liu, G. T. Park, L. Cavallo, L. Wang, H. N. Alshareef, Y. K. Sun, J. Ming, *Adv. Mater.* **2021**, *33*, 2005993.
- [42] Q. Li, Z. Cao, W. Wahyudi, G. Liu, G.-T. Park, L. Cavallo, T. D. Anthopoulos, L. Wang, Y.-K. Sun, H. N. Alshareef, J. Ming, *ACS Energy Lett.* **2020**, *6*, 69.
- [43] a) L. Xing, O. Borodin, *Phys. Chem. Chem. Phys.* **2012**, *14*, 12838; b) O. Borodin, M. Olguin, C. E. Spear, K. W. Leiter, J. Knap, *Nanotechnology* **2015**, *26*, 354003; c) C. D. Malliakas, K. Leung, K. Z. Pupek, I. A. Shkrob, D. P. Abraham, *Phys. Chem. Chem. Phys.* **2016**, *18*, 10846; d) Y. Zheng, P. B. Balbuena, *J. Chem. Phys.* **2021**, *154*, 104702.
- [44] a) K. Xu, *Chem. Rev.* **2004**, *104*, 4303; b) K. Xu, *Chem. Rev.* **2014**, *114*, 11503; c) N. Piao, S. Liu, B. Zhang, X. Ji, X. Fan, L. Wang, P.-F. Wang, T. Jin, S.-C. Liou, H. Yang, J. Jiang, K. Xu, M. A. Schroeder, X. He, C. Wang, *ACS Energy Lett.* **2021**, *6*, 1839.